Polymerization-Induced Self-Assembly (PISA) for in situ drug encapsulation or drug conjugation in cancer application

Hien Phan, Mélissande Cossutta, Claire Houppe, Clémence Le Cœur, Sylvain Prevost, Ilaria Cascone, José Courty, Jacques Penelle, Benoit Couturaud

Polymerization-Induced Self-Assembly (PISA) for *in situ* drug encapsulation or drug conjugation in cancer application

Hien Phan [a], Mélissande Cossutta [b], Claire Houppe [b], Clémence Le Cœur [a,c], Sylvain Prevost [d], Ilaria Cascone [b,e], José Courty [b,e], Jacques Penelle [a], Benoit Couturaud [a,*]

[a] *Univ Paris Est Créteil, CNRS, Institut de Chimie et des Matériaux Paris-Est (ICMPE), UMR 7182, 2 rue Henri Dunant, 94320 Thiais, France*
[b] *INSERM, U955, Immunoregulation and Biotherapy, F-94000, Créteil, France*
[c] *Laboratoire Léon Brillouin, CEA-CNRS (UMR-12), CEA Saclay, Université Paris-Saclay, 91191 Gif-sur-Yvette Cedex, France*
[d] *Institut Laue-Langevin, 71 Avenue des Martyrs, 38042 Grenoble, France*
[e] *AP-HP, Groupe hospitalo-universitaire Chenevier Mondor, Centre d'investigation clinique Biothérapie, F-94010 Créteil, France*

GRAPHICAL ABSTRACT

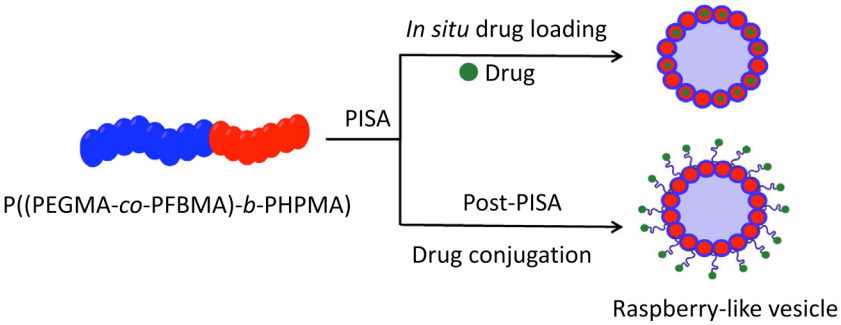

Keywords:
polymerization-induced self-assembly (PISA)
Block copolymers
Drug-loaded nanoparticles
Polymer-drug conjugates

ABSTRACT

Hypothesis: We describe the possibility of using the same block copolymer carriers prepared by PISA for *in situ* drug encapsulation or drug conjugation.
Experiments: Block copolymers containing poly((ethylene glycol) methacrylate)–*co*-poly (pentafluorophenyl methacrylate)-*b*-poly(hydroxypropyl methacrylate) (P((PEGMA-*co*-PFBMA)-*b*-PHPMA)) were synthesized at 10 wt% using PISA. The first approach involved *in situ* Doxorubicin (DOX) loading during PISA, while the second exhibited surface functionalization of PISA-made vesicles with dual drug therapies, *N*-acetyl cysteine (NAC) and DOX using *para*-fluoro-thiol reaction (PFTR) and carbodiimide chemistry, respectively. Cytotoxicity, cell uptake, and cell apoptosis were assessed on MDA-MB-231 cell lines.
Findings: P((PEGMA-*co*-PFBMA)-*b*-PHPMA) nanocarriers were prepared, showing size and shape transformations from spheres, cylinders to raspberry-forming vesicles. DOX was readily loaded into NPs during PISA with relatively high encapsulation efficiency of 70 %, whereas the plain PISA-made vesicles could be functionalized with NAC and DOX at high yields. DOX-free NPs showed biocompatibility, whilst DOX-conjugated NPs imparted a concentration-dependent cytotoxicity, as well as an enhanced cell uptake

Abbreviations: PISA, polymerization-induced self-assembly; NP, nanoparticle; P((PEGMA-*co*-PFBMA)-*b*-PHPMA), poly((ethylene glycol) methacrylate)–*co*-poly (pentafluorophenyl methacrylate)-*b*-poly(hydroxypropyl methacrylate); E, PEGMA; F, PFBMA; H, HPMA; DOX, doxorubicin; NAC, *N*-acetyl cysteine; PFTR, *para*-fluoro-thiol reaction.

* Corresponding author.
E-mail address: benoit.couturaud@cnrs.fr (B. Couturaud).

compared to free DOX. The results demonstrated that the same PISA-derived self-assemblies enabled either *in situ* drug encapsulation, or post-polymerization surface engineering with useful functionalities upon tuning the macro-CTA block, thus holding promises for future drug delivery and biomedical applications.

1. Introduction

In response to more complex and challenging biomedical applications, it is becoming increasingly important to design highly functional polymer materials whose macromolecular architectures and colloidal properties should be well controlled and characterized, but without laborious and costly synthetic procedures. One possible solution is to employ amphiphilic diblock copolymers that can self-assemble in aqueous media to generate drug delivery vehicles, while their block chemistries and inherent physicochemical properties can be readily tuned to engineer NPs precisely tailored to specific biomedical applications. [1,2] Block copolymer assemblies can be typically prepared using conventional formulation methods such as nanoprecipitation or thin-film hydration, though these techniques can limit multiple purification steps and avoid the additional use of toxic surfactants, many challenges still exist that hamper its scope for commercial perspectives. For example, very low polymer concentrations are used (<1 wt-%), the self-assembly takes place following some post-polymerization procedures, and obtaining higher order morphologies is empirically difficult. It is thereby critical to generate processes that are compatible with future industrialization using efficacious, economic, and environmentally friendly synthetic routes. In this regard, polymerization-induced self-assembly approach (PISA) has increasingly emerged that facilitates both polymerization and *in situ* self-assembly straightforward in one pot, while obtaining NPs at remarkably high concentrations (a current maximum of 50 wt%) with several sizes and morphologies (spheres, cylinders and vesicles) being accessible. [3–5] PISA typically involves the chain extension of a living solvophilic polymer precursor named macro-chain transfer agent (macro-CTA), with a monomer, forming amphiphilic block copolymer particles, either through dispersion or emulsion methods in polar (water, ethanol) or nonpolar solvents (*n*-alkanes). [6] PISA-prepared NPs are mostly obtained by reversible addition-fragmentation transfer (RAFT) living polymerization techniques due to their solvent and monomer versatilities, [7] especially PISA via RAFT emulsion in water is an environmentally friendly approach.

Despite a myriad of research advances on PISA for drug delivery and biomaterials sciences, there have been relatively a few reports to date on a PISA-developed system that is versatile to both drug encapsulation and conjugation. The current work therefore focuses on exploiting the possibility of (i) *in situ* physical drug encapsulation during PISA; (ii) tuning the external hydrophilic macro-CTA block for post-PISA dual drug conjugations aiming at enhancing therapeutic effects. To this end, drug encapsulation experiment will be carried out using DOX. On the other hand, NAC and DOX, in turn will be conjugated onto PISA-made NPs using *para*-fluoro-thiol and carbodiimide reaction, as the combination use of NAC and DOX was reported to reduce chemotherapy-induced resistance and aggressiveness in triple-negative breast cancer (TNBC) [8] and can attenuate the harshness of DOX-caused cardiotoxicity. [9] To facilitate drug conjugations into polymer NPs, it is necessary to integrate functional moieties in the macro-CTA that can enable the interactions of outer hydrophilic layer with drug molecules at high yields. One possible strategy is to use a fluorine-bearing polymer block in the macro-CTA, e.g. poly(2,3,4,5,6-pentafluorobenzyl methacrylate) (PFBMA) as its *para*-fluorines can be readily substituted by amines, thiols and carbonylthiolates. [10–14] Finally, cell viability and cell uptake will be assessed on MDA-MB-231 cell lines.

2. Materials and methods

Experimental materials and characterization are described in detail in Supporting Information (SI).

2.1. Synthesis of poly((ethylene glycol) methacrylate)–co-poly (pentafluorophenyl methacrylate) macro-CTA (P(PEGMA-co-PFBMA))

PFBMA was synthesized as described in section 3.1 in SI. The ^{19}F-containing copolymer P(PEGMA475-*co*-PFBMA) was synthesized using RAFT polymerization in the presence of CEPA-F CTA (see procedures in section 3.2 in SI) and AIBN initiator in dioxane. It was aimed to investigate the impacts of hydrophilic blocks on final PISA-made particle sizes, thereby different chain lengths of the hydrophilic macro-CTA were prepared by (i) varying the ratios of PEGMA475 to PFBMA in the co-polymerization in which PFBMA accounted for 10 wt% and 20 wt%; (ii) varying different degrees of polymerization (DP) of both methacrylate-based reactive agents PEGMA475 and PFBMA to CTA or changing the ratio of [PEGMA475:PFBMA] to CTA, thus, DPs of [PEGMA475 and PFBMA] to CEPA-F CTA were as follows: 40:1; 80:1; 120:1; 150:1. Different AIBN concentrations and temperatures were also investigated as they are critical to the polymerization reactions. All the studied conditions are described in Table SI1. Initially, adequate amounts of PEGMA475, PFBMA, CEPA-F CTA, AIBN and dioxane were added into a Schlenk tube containing a magnetic stirrer. The solution was degassed using freeze–pumpthaw cycles (3 times) and then heated to 70 or 80 °C in an oil bath under stirring. Samples were taken periodically every 45 min with deoxygenated syringes and examined under ^{1}H NMR, ^{19}F NMR ($CDCl_3$) and SEC (DMF, PMMA standard) to calculate the conversion and assess the polymerization kinetics. In the end, the polymerization was quenched by rapid cooling upon immersion of the flask in a liquid N_2 bath. The solution was purified by dialysis (deionized water, Mw = 3500 g mol^{-1}) for 48 h then freeze-dried to afford the yellow oil product.

The monomer conversion at a given polymerization time was determined by comparing the area of the polymer peaks to that of the remaining monomer peaks, for example comparing the peaks of ethylene groups in PEGMA and the peaks of pentafluorophenyl ester groups in PFBMA. Subsequently, the monomer conversion, the initial $[M]_0$:$[CTA]_0$ ratio were used to calculate the theoretical DP.

PEGMA and PFBMA were shorted as E and F, respectively. We conducted the kinetics at each DP and investigated the influences of AIBN and temperatures on the polymerization to choose the most linear and controllable kinetics. Figure SI3 presents 5 kinetics (kinetics of $E_{96}F_{24}$ was shown in the main text) showing the highest control over the polymerization of PEGMA and PFBMA with

CTA. Table SI2 summarizes these 6 copolymers and their corresponding reaction parameters.

2.2. Polymerization-Induced Self-Assembly (PISA) of P(PEGMA-co-PFBMA) macro-CTA and hydroxypropyl methacrylate (HPMA)

HPMA, macro-CTA and V-50 were placed in a vial and dissolved in deionized H_2O at the ratio of [HPMA]:[P(PEGMA475-*co*-PFBMA)]:[V-50] = 300:1:0.2 . The vial was sealed with rubber septum and purged with argon for 30 min. After degassing, the reaction was performed in a preheated oil bath at 52 °C for 6 h. The polymerization was quenched by cooling the mixture rapidly and exposure to air. Samples were withdrawn every 15 min using deoxygenated syringes to study the reaction kinetics, examined under ^{1}H, ^{19}F NMR (DMSO), SEC (PMMA standard, DMF), DLS, and TEM.

2.3. In situ drug loading

Preparation of stock solutions of DOX: To a glass vial, DOX·HCl red powder was mixed with TEA (1:8 mol eq) in DCM (1 mg mL^{-1}) to improve the hydrophobicity of DOX, stirred and placed in the dark for 4 h until a complete solution then the vial was evaporated to remove DCM. The $E_{74}F_{19}$ macro-CTA was chain-extended with HPMA at 10 wt% solid contents in dioxane, using V-50 initiator at 52 °C. The mixture of DOX and $E_{74}F_{19}$ was prepared at multiple feed weight ratios (DOX/block copolymer fwr%): 0.1, 0.2, 0.3, 0.5, 0.7, which in turn resulting in numerous reaction compositions as follows: [HPMA]/[$E_{74}F_{19}$]/[DOX]/[V-50] = 300/1/0.1/0.4, 300/1/0.3/0.4, 300/1/0.4/0.4, 300/1/0.7/0.4, 300/1/1/0.4. In a 10 mL glass vial, $E_{74}F_{19}$ (100 mg, 2.46 μmol) was dissolved in 1.95 mL of deionized water. DOX (1 mg) after evaporation of DCM was dispersed and mixed well in a HPLC vial containing HPMA (107 mg, 740 μmol). The solution of DOX and HPMA was then added dropwise to the above 10 mL vial. Finally, V-50 (134 ug, 0.49 μmol) was added to the previous solution. The vial was sealed and degassed under argon in an ice/water bath for 30 min. The polymerization was conducted at 52 °C for 6 h. The resulting drug-loaded NPs were recovered by dialysis (MWCO 3500 g mol^{-1}, deionized water) for 48 h to remove free drug. The purified DOX-encapsulated NPs were lyophilized and the obtained solid was dissolved in DMSO to quantify the loaded DOX by comparing the UV absorbance at 485 nm of this sample to a standard calibration curve of DOX in DMSO. The drug loading (DL %) and encapsulation efficiency (EE %) was calculated as:

$$Drugloading(DL\%) = \frac{Amountofloadeddrug}{TotalNPamount} * 100$$

$$Encapsulationefficiency(EE\%) = \frac{Amountofloadeddrug}{Initialdrugamount} * 100\%$$

2.4. Post-PISA drug conjugation

2.4.1. Para-Fluoro-Thiol reaction (PFTR) of P((PEGMA-co-PFBMA)-b-PHPMA) NPs with NAC

The reaction was conducted with adjustments following a protocol proposed by Turgut et al. [13] The reaction was attempted at different ratios of pentafluorophenyl (PFP) unit to NAC molecules, including 1:10, 1:30, 1:50, 1:60, 1:80, 1:120. At the ratio of 1:60, for example, 0.179 g (1.1 mmol) NAC and 0.178 g ($2.29x10^{-3}$ mmol, 4 mL) $E_{82}F_{10}$-H_{300} NP solution were mixed in a vial, adjusted to pH 13 by 9.5 mL NaOH 0.4 M solution, and stirred for 15 min at room temperature until complete dissolution, then sealed with a rubber septum. Thiols are most likely to undergo oxidation to form disulfide bonds upon exposure to ambient conditions, thus the reaction were conducted in degassed media by purging with Argon for 30 min. The solution was placed in a pre-heated oil bath at 50 °C. After 72 h, excess of NAC was purified by dialysis (deionized water, 3500 g mol^{-1}) for 48 h. The final solution was examined under ^{1}H, ^{19}F NMR (D_2O), SEC (PMMA standard, DMF), DLS and TEM.

2.4.2. Coupling of DOX into NAC-linked NPs using EDC/NHS activation reaction

DOX was subsequently conjugated on the NPs through interacting with NAC moieties based on two-step protocol. [15] The first step involved activating the carboxylic groups of NAC by NHS-carbodiimide chemistry. Briefly, 4.1 mg P(($PEGMA475_{74}$-*co*-$PFBMA_{19}$)-*b*-$PHPMA_{300}$) ($E_{74}F_{19}$-H_{300}) NP (0.48 μmol, 0.0137 mg/mL) was dispersed in 3 mL of deionized water containing 0.92 mg EDC (4.8 μmol) and 1.1 mg NHS (9.59 μmol) under moderate stirring at ambient temperature for 3 h. The molar ratio of NP:EDC:NHS was kept at 1:10:20. Later, DOX (0.278 mg, 0.48 μmol) was added to the above solution at the ratios of NP:DOX at 1:1 and 1:5, and incubated for 12 h under moderate stirring. The solution was then purified by dialysis (deionized water, 3500 g mol^{-1}) for 48 h to remove free DOX. Sample was freeze-dried for 24 h and the amount of DOX conjugated on NP surface was quantified by dissolving the obtained solid in a known volume of DMSO and comparing this solution with the calibration curve of DOX in UV measurement at 485 nm in DMSO.

2.5. Cell culture experiments

2.5.1. In vitro cell viability

Cell viability was studied using AlamarBlue assay for NPs and NPs-NAC as well as MTT assay for free DOX and DOX-coupled NPs. Briefly, human triple negative breast cancer cell line (MDA-MB-231) were harvested by trypsin via physical scraping. Cells were washed with PBS, resuspended in a DMEM medium supplemented with 10 % of fetal calf serum (complete DMEM), and seeded into a 96-well plate at a concentration of 1 × 5000 cells per well in 100 μL of the complete DMEM medium. The cells were then incubated for 24 h prior to analysis. For a typical test, the cells were incubated for 72 h in a fresh complete DMEM medium containing samples at designed concentrations: 31.3–1000 μg mL^{-1} for NPs and NP-NAC (equivalent NP concentration) or 0.022 – 3.9 μg mL^{-1} for DOX, DOX-loaded NPs, and NP-NAC-DOX (equivalent DOX concentration). Three parallel wells were set for each concentration. After incubation, AlamarBlue reagent (10 μL, 5 mg mL^{-1}) or MTT (20 μL, 5 mg mL^{-1}) was added into each well. After an additional incubation for 4 h, the fluorescent intensity of AlamarBlue assay was measured at Ex/Em 560/590 nm and the absorbance of MTT assay was measured at 595 nm.

2.5.2. Cell uptake studies

MDA-MB-231 cells were cultured on micro slide 24-well chambers (Ibidi, Germany) at a density of 1 × 50000 cells per well for 24 h in DMEM supplemented with 10 % fetal calf serum. Cells were then exposed to DOX and NP-NAC-DOX at a DOX concentration of 0.35 μg mL^{-1} in the dark at 37 °C and 5 % CO_2 for 5 h and 72 h. Cells were then fixed with 4 % formaldehyde (in PBS) for 10 min and washed with PBS (three times). Cells were then treated with PBS-Triton 0.1 % for 10 min and washed with PBS (three times). Later, cells were incubated with diamidino-2-phenylindole (DAPI) nuclei stain at the concentration of 1 μg mL^{-1} for 15 min in the dark at RT and washed with PBS (three times). Cells were imaged with a Zeiss LSM 900 Confocal Laser Scanning Microscope. Image J Software was utilized for image processing.

2.5.3. Apoptosis assay by Incycute® live-cell analysis

Annexin V dye (Ex. Max 593 nm/Ex. Min 614 nm) was dissolved in 100 μL of PBS as stock solution. 100 μL of MDA-MB-231 cells were cultured on each well in a 96-well plate at a density of 1 × 5000 cells per well for 24 h in DMEM supplemented with 10 % fetal calf serum. The cell plate was removed from the incubator and aspirate off the culture medium. Cells were incubated with free DOX and NP-NAC-DOX at the same DOX concentration of 0.35 μg mL^{-1}. The untreated cells were used as a control. Annexin V dye was added to each well for a final dilution of 1:200. The cell plate was placed into the Incucyte® Live-cell Analysis System to monitor apoptosis using green fluorescence channel for DOX and red channel for Annexin V dye. Each well was scanned every 2 h within 72 h. Data was analyzed using the integrated IncuCyte software version 2021A.

3. Results and discussion

3.1. Synthesis of poly((ethylene glycol) methacrylate)–co-poly (pentafluorophenyl methacrylate) macro-CTA (P(PEGMA-co-PFBMA))

PEGMA and PFBMA were co-polymerized using CEPA-F, a specially designed CTA bearing a fluorine moiety that facilitates NMR signal assignments and conversion calculations. The RAFT polymerization of PEGMA and PFBMA in dioxane using AIBN as initiator is depicted in (Fig. 1A). The effect of temperature, AIBN concentration, and [PEGMA]:[PFBMA] feed molar ratios on the resultant polymers were examined to obtain the most controlled parameters for the polymerization. All parameters and the corresponding features for the synthesized polymers are presented in Table SI1 and SI2. Fig. 1 displays the kinetic profile of $PEGMA475_{74}$-*co*-$PFBMA_{19}$ (abbreviated as $E_{74}F_{19}$). The polymerization rate of $E_{74}F_{19}$ increases linearly up to 135 min with approximately 80 % conversion for both monomers, then tends to stabilize to around 90 % until 360 min (Fig. 1B). *SEC* traces of $E_{74}F_{19}$ copolymers at various polymerization times are unimodal with M_w/M_n polydispersity values from 1.20 to 1.22 and the relative molecular weights gradually shifting to higher values over time. Molecular weights and conversions do not evolve significantly after 135 min, thereby, the reaction was quenched at 135 min to ensure that the obtained polymers were in the most controllable architectures. The same approach was applied to the other polymerizations, and by following their kinetics the reactions were quenched when their respective conversions are stabilized. Table SI2 presents six polymers along with their corresponding reaction parameters, which were selected upon the most linear and controllable kinetics. It indicates that polymers with low DPs such as DP 40 and 80 need a lower AIBN concentration (0.1 eq.) and a lower temperature (70 °C) to be fully activated (except for $PEGMA_{64}$-*co*-$PFBMA_{16}$ at 80 °C). In the meanwhile, more AIBN (0.2 eq.) and a higher temperature (80 °C) are necessary to initiate reactions with high DPs such as DP 120 and 150. Table SI3 summarizes the characteristics of six P (PEGMA-*co*-PFBMA) polymers obtained by RAFT in dioxane under various reaction conditions.

3.2. Polymerization-Induced Self-Assembly (PISA) of P(PEGMA-co-PFBMA) macro-CTA and hydroxypropyl methacrylate (HPMA)

3.2.1. Effect of varying macro-CTA lengths on particle size

The synthesized macro-CTA was then chain-extended with the HPMA monomer targeting a DP of 300 and using V-50 initiator at 52 °C in deionized water. In fact, previous literature has extensively focused on investigating the effect of changing DP or hydrophobicity on the particle size, [16–19] whereas very little was known about how changing the water-soluble moieties can exert an impact on the particle size. Therefore, the polymerization of HPMA was carried out in a one-pot PISA approach using different lengths of macro-CTAs while keeping the length of HPMA constant to study the impact of amphiphilic balance on particle size. Numerous macro-CTAs were used: the first group containing PFBMA 10 wt% includes $E_{50}F_6$ and $E_{82}F_{10}$; the second group containing PFBMA 20 wt% includes $E_{22}F_5$, $E_{46}F_9$, $E_{74}F_{19}$, and $E_{94}F_{23}$. Table SI4 summarizes the results of these 6 block copolymer NPs prepared by PISA and their characteristics. Fig. 2 exhibits that at both PFBMA 10 wt% (Fig. 2A) and 20 wt% (Fig. 2B), despite keeping HPMA constant and increasing the macro-CTA, the particle sizes

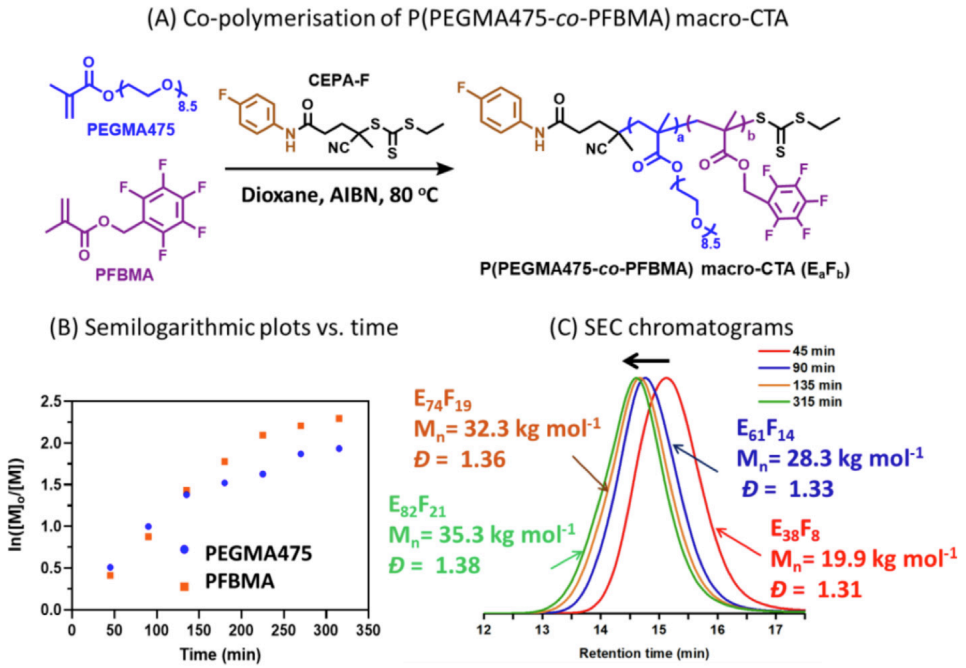

Fig. 1. (A) Schematic diagram of the co-polymerization of P(PEGMA-*co*-PFBMA) macro-CTA DP120; Kinetic plots of RAFT polymerization of PEGMA with PFBMA in dioxane at 80 °C: (B) Semilogarithmic plots vs. time; (C) *SEC* chromatograms (DMF, PMMA standard). PEGMA was denoted as E, PFBMA was denoted as F.

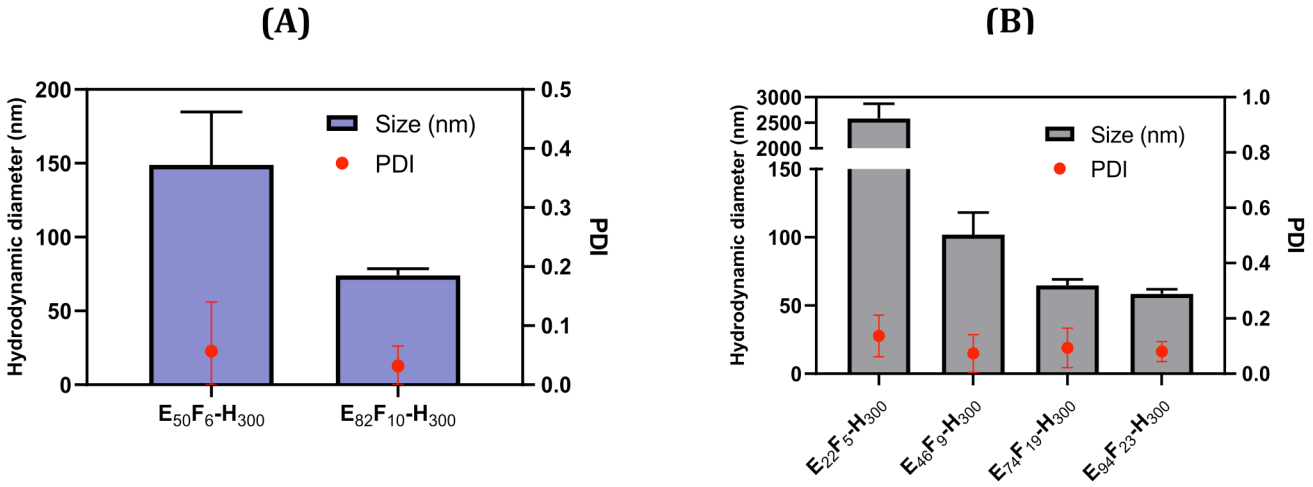

Fig. 2. Size and PDI of NPs prepared by PISA with HPMA using different macro-CTAs. (A) PFBMA 10 wt%, (B) PFBMA 20 wt%. Results are shown as the mean ± standard deviation of three replicates.

tend to decrease. For example, particles of $E_{22}F_5$-H_{300} result in precipitation of over 2 μm and very large size distribution with PDI 0.9, however, higher macro-CTA of $E_{94}F_{23}$-H_{300} generates NPs of 60 nm and PDI 0.21. The mixture also became less turbid when increasing the water-soluble blocks. This could be simply explained that at the same hydrophobic lengths and lower hydrophilicity, the mixture is likely to be more hydrophobic, forming larger particles and precipitation. However, longer hydrophilic segments with the same hydrophobic blocks cause the hydrophilic to hydrophobic equilibrium to increase, more hydrophilic chains are inserted to stabilize the hydrophobic block and decrease particle size. [20] Our observation is also supported by Yang et al. whereby the particle size can be tuned by adjusting the ratio of hydrophilic to hydrophobic block, with lower hydrophilicity leading to larger vesicles and smaller polymer shells. [21] That being said, particle size could be readily tuned by adjusting the hydrophilic blocks while remaining the hydrophobic blocks unchanged. From Fig. 2 three block copolymers were selected for further experiments, including $E_{82}F_{10}$-H_{300}, $E_{74}F_{19}$-H_{300}, and $E_{94}F_{23}$-H_{300} as their sizes are <100 nm with narrow size distributions that can facilitate drug delivery in biological cell environment. [22,23]

3.2.2. PISA kinetics of $E_{74}H_{19}$ macro-CTA with HPMA

Next, the polymerization kinetics was implemented using $E_{74}H_{19}$ macro-CTA with HPMA at DP300 and 10 wt% of total solid contents, with V-50 at 52 °C in H_2O. At predetermined times, samples were extracted using deoxygenated syringes to obtain the kinetic profiles of the PISA. The process was monitored by ^{1}H NMR, DLS, TEM and *SEC* as explained above; results are listed in Fig. 3, as well as detailed information on monomer conversions, DPs, molecular weights, and DLS measurements are summarized in Table SI5. Monomer conversion is complete within 6 h. Fig. 3B exhibits the monomer conversion (%) and semilogarithmic plot of PISA process, showing two regimes: (i) a slow reaction rate up to 1 h: including the formation of spherical micelles at 0.5 h with 9 % conversion and DP_{HPMA} = 27 (TEM of Fig. 3F1), and these spherical particles appear to elongate into cylinders at 0.75 h with 13 % conversion and DP_{HPMA} = 40 (Fig. 3F2), the conversion later increases to 17 % with DP_{HPMA} = 51 at 1 h when these cylinders seem to assemble toward premature vesicles, (Fig. 3F3); (ii) the second stage involves a gradually increasing conversion to 100 % until 4 and 6 h when complete vesicles are ultimately formed. In fact, the chain extension of macro-CTA agent with solvophobic monomers usually begins with the formation of spherical micelles with the smallest packing parameter p < 1/3, as the degree of polymerization (DP) increases, spheres are transformed to worm-like, cylinders or fibers with increasing p from 1/3 < p < 1/2, accommodating the increasing monomers, which are eventually transitioned to bilayer structures like vesicles with p > 1/2, containing the highest number of monomers into the self-assembled NPs. [24,25] Fig. 3 F2 and F3 indicate TEM images of very rigid cylindrical micelles, very close to nanofibers. We suppose that the high rigidity of cylinders is probably due to the almost doubled increase of DP_{HPMA} from 27 to 51 at 0.5 h and 1 h, respectively, explaining that increasing hydrophobicity tends to stabilize the cylindrical forms and make them less mobile, thereby forming a very rigid and straight structure.

The lone macro-CTA $E_{74}F_{19}$ made up of hydrophilic PEGMA and hydrophobic PFBMA could indeed, readily self-assemble into NPs in water due to the fluorine atom's high electronegativity and PFBMA's low surface energies and high aqueous insolubility, producing self-assemblies of 269 nm but very high PDI of 1, Figure SI5. [26] Such large dispersity might be owing to the inadequate polymer' amphiphilic balance, with larger PEGMA vs. PFBMA. However, the chain extension of such macro-CTA with HPMA through PISA led to a structural reorganization of NPs to a newly equilibrated hydrophilic-to-hydrophobic ratio, thus reducing particle sizes and PDIs. Therefore, following the reaction with HPMA, NPs of 44 nm are initially formed at 0.5 h, whose sizes increase to 62 nm at 0.75 h, and eventually remain stable at 69 nm until the monomer conversion reaches 100 % (Fig. 3D). DLS size distribution profiles indicate that particle sizes increase when increasing DP of HPMA while polydispersity indices decrease. The size distribution (PDI) decreases from 0.18 to 0.02 as particle size increases from 44 nm to 69 nm, indicating that NPs become more homogenous at the end of the polymerization process.

SEC chromatograms of $E_{74}F_{19}$ with HPMA show characteristic peaks with polydispersity values in the 1.32 – 1.59 range, confirming the relative controllability of PISA (Fig. 3E). The particle size and shape transformations are in accordance with the increasing monomer conversions as well as the increasing NMR and *SEC*'s molecular weights (Fig. 3B, 3C), which falls in line with general PISA behavior described in previous reports. [27–29] Consequently, the polymerization of HPMA with fluorinated macro-CTA by PISA could be used to synthesize $E_{74}F_{19}$-H_{300} vesicles of 69 nm and PDI of 0.02.

3.3. In situ drug encapsulation

Initially, the hydrophilic form of DOX.HCl was entrapped into NPs through PISA, however, obtaining a very low encapsulation efficiency of 18 %. Therefore, by adapting from previous literature,

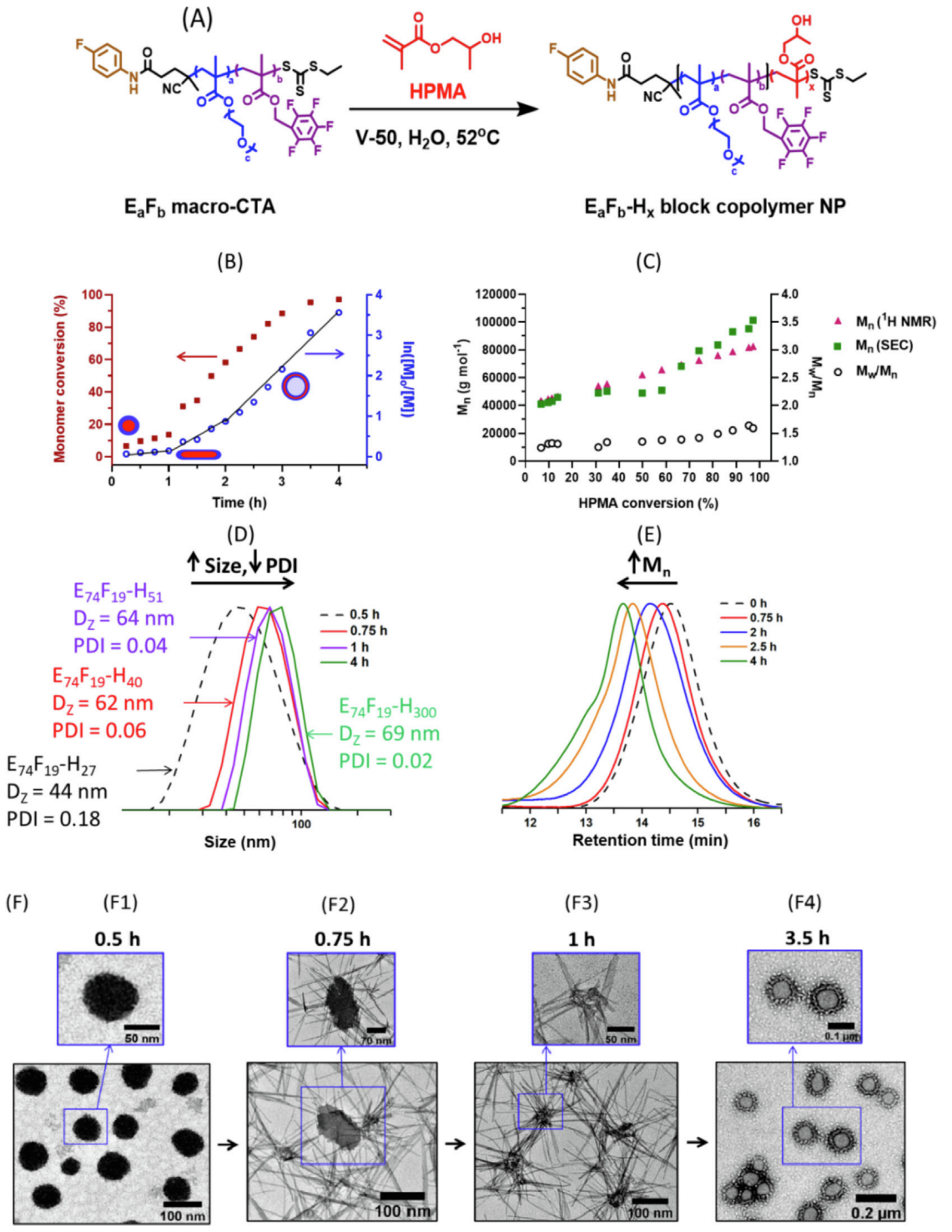

Fig. 3. (A) Diagram of PISA of HPMA (HPMA abbreviated as H) and $E_{74}H_{19}$ macro-CTA at 52 °C, 10 wt% solids, and DP300; (B, C, D, E) Kinetics plots of the PISA process: (B) Monomer conversion and semilogarithmic plots vs. time; (C) Number-average molecular weight M_n determined by ^{1}H NMR ($CDCl_3$), *SEC* and dispersity vs. HPMA conversion (%); (D) DLS spectra by normalized intensity (%); (E) *SEC* chromatograms (PMMA standard, DMF). (F) TEM at 0.5 h, 0.75 h, 1 h and 3.5 h during the PISA reaction.

DOX.HCl was treated with triethylamine (TEA) (DOX:TEA = 1:8) in DCM to increase its hydrophobicity, thus enhancing its solubility in water-miscible HPMA monomers to possibly increase the drug loading. [30,31] DOX was simultaneously encapsulated during the formation of NPs by PISA simply by mixing all the reactive components, macro-CTA, drug, HPMA and initiator in one pot. The loading was confirmed, by simply observing a visual color change from transparent red in the initial solution to turbid red after PISA which remains the same color following 48-h dialysis, thus indicating the formation of NPs encapsulated with DOX (Fig. 4). DOX was loaded into NPs at various feed weight ratios (fwr%) (Table 1), showing relatively high encapsulation efficiency (EE%) for a maximum of around 70 %. As the concentrations of DOX increase their respective sizes increase, while zeta potentials remain neutral. These results suggest that DOX could be readily encapsulated during PISA in one pot, obtaining final vesicles at high concentration of 10 wt%, small and homogeneous particle size (<100 nm, PDI < 0.2), as well as acceptable encapsulation efficiencies, compared to previous reports. [30,31] Additionally, DOX was indicated to remain its stability in harsh condition of PISA loading

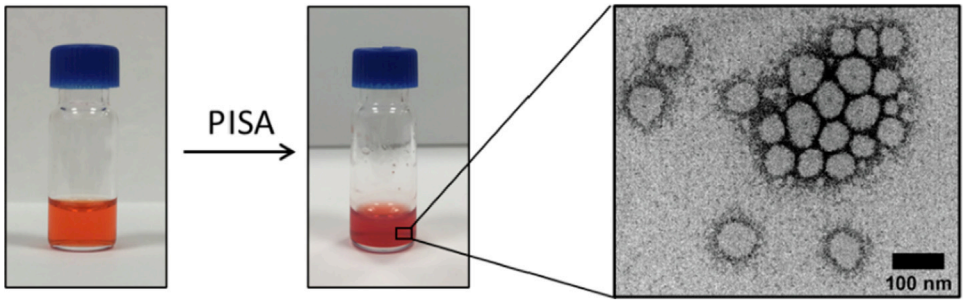

Fig. 4. Visual color change from free DOX (clear red) to DOX-loaded NPs (turbid red) after PISA and TEM image of DOX-loaded NPs at fwr% of 0.3.

Table 1
Characteristics of DOX-loaded NPs during PISA.

DOX/NP fwr%[a]	Conv. (%)[b]	DP[c]	DL (%)	EE (%)	D_Z (nm)	PDI	ZP (mV)
0	NA	NA	NA	NA	68.9 ± 3.1	0.04 ± 0.01	−1.11 ± 0.8
0.1	97	291	0.06 ± 0.01	66.5 ± 8.7	64.2 ± 2.7	0.08 ± 0.05	−3.32 ± 1.7
0.2	96	288	0.11 ± 0.02	69.6 ± 6.4	63.9 ± 5.0	0.09 ± 0.08	−0.67 ± 2.3
0.3	84	252	0.19 ± 0.05	67.8 ± 2.0	80.4 ± 10.0	0.09 ± 0.03	0.34 ± 2.7
0.5	90	270	0.32 ± 0.04	66.1 ± 4.1	96.3 ± 6.7	0.08 ± 0.04	1.27 ± 2.5
0.7	89	267	0.43 ± 0.04	64.3 ± 4.9	102.8 ± 5.7	0.07 ± 0.06	0.81 ± 1.9

[a] Initial feed weight ratio % of DOX to NP;
[b] Calculated from ^{1}H NMR;
[c] DP = Conversion (%) × initial DP 300

reaction at 52 °C for 6 h, as the DOX-loaded NPs exhibit the same UV absorbance spectrum as free DOX.HCl and DOX.TEA (Figure SI6). This result is in line with recent reports on the stability of DOX from PISA-inspired *in situ* DOX loading, at even higher temperature of 70 °C by Malmstrom and co-workers. [30,31]

3.4. Post-PISA drug conjugation

In addition to the *in-situ* drug encapsulation, we attempted to further exploit post-PISA surface functionalization using chemistries associated with the external hydrophilic macro-CTA. This second part will be particularly discussing the particle surface conjugation with NAC and DOX in water.

3.4.1. Para-Fluoro-Thiol reaction (PFTR) of P((PEGMA-co-PFBMA)-b-PHPMA) NPs with NAC

In the next step of the synthetic design, *N*-acetylcysteine (NAC) was added as its thiol group can react with *para*-fluorine atoms of the polymer-attached pentafluorophenyl (PFP) rings using *para*-Fluoro-Thiol Reaction (PFTR). Three out of the above six block copolymer NPs having the smallest particle sizes selected from Fig. 2, were coupled with NAC *via* PFTR, namely $E_{82}F_{10}$-H_{300}, $E_{74}F_{19}$-H_{300}, and $E_{94}F_{23}$-H_{300}. A procedure published in the literature was used systematically. [13] In our study, $E_{82}F_{10}$-H_{300} and NAC were mixed at several ratios, with one PFP unit corresponding to 10, 30, 50, 60, 80 or 120 NAC molecules, respectively, to determine optimal conditions for full conversion.

Providing that the reaction environment is oxygen-free to prevent the formation of oxidized disulfide groups, the thiol nucleophile in NAC is expected to attack and substitute the electron-deficient carbon at the *para* position of the pentafluorophenyl moiety. The PFP segment of $E_{82}F_{10}$-H_{300} bears *ortho*, *meta*, and *para* fluorine atoms whose signals are displayed as three distinct chemical shifts in ^{19}F NMR (Fig. 5A). A successful incorporation is obtained when the peak at the *ortho* position (141 ppm) is maintained while the *para* one (152 ppm) disappears, and the *meta* one (161 ppm) moves towards a higher chemical shift (134 ppm). At ratios of 1:10 and 1:30, the *para* fluorine signal was still present. Increasing to 1:50, 1:60, and 1:80, the *para* fluorine was completely removed,

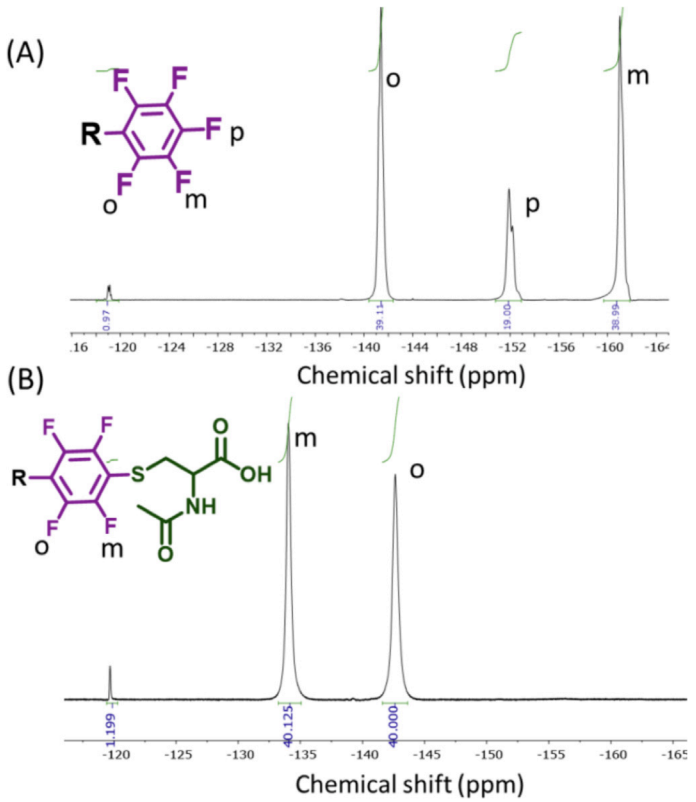

Fig. 5. ^{19}F NMR spectrum of $E_{74}F_{19}$-H_{300} (D_2O) (A) before and (B) after NAC conjugation. R: NP.

the signal for the *ortho* fluorine remained at the same position and the *meta* one moved to 134 ppm, indicating that NAC was fully linked to the para position of PFP motifs of block copolymer. Thus, we assumed that a higher ratio of PFP unit to NAC might be expected to increase the reaction kinetics and improve the yields. Nonetheless, when increasing to the ratio of 1:120, the spectrum still showed the initial peaks for all three types of fluorine at the

same chemical shifts as compared with those in the initial block copolymer. This failure results most probably from the impossibility to maintain the high required pH when using large excesses of acidic reagents such as NAC. Indeed, one important aspect to the success of a PFTR between NAC and a PFP motif is the pH of aqueous media as the reactive species corresponding to NAC evolve with the pH from a neutral NAC to a monoanion, as a result of the transformation of the carboxylic acid to a carboxylate, and finally to a dianion based on the further removal of a proton on the thiol. Thereby, a solution with a pH value higher than pKa of the NAC thiol (9.52) is needed to facilitate the reaction by replacing the initial thiol with a much more nucleophilic thiolate. [32] A ratio of 1 PFP unit to 60 equivalents of NAC was hence applied to $E_{74}F_{19}$-H_{300} and $E_{94}F_{23}$-H_{300} that showed quantitative NAC integration into the particles. Fig. 5 exhibits ^{19}F NMR (D_2O) spectrum of $E_{74}F_{19}$-H_{300} conjugated with NAC at a ratio of 1:60.

NAC conjugation was also confirmed by zeta potential (ZP) measurements at neutral pH (Fig. 6E). While $E_{82}F_{10}$-H_{300} NPs with no external charges have a ZP of −0.75 mV, NAC-coupled $E_{82}F_{10}$-H_{300} particles impart a ZP of −10.20 mV, indicating that the particle surface is negatively charged attributed to the carboxyl groups (COO–) grafted onto the polymeric vehicles. Similarly, the initial, neutral $E_{74}F_{19}$-H_{300} NPs have a ZP of −0.96 mV, which decreases to −19.90 mV after NAC insertion.

Particle sizes after NAC insertion slightly increase for $E_{82}F_{10}$-H_{300} from 71.8 to 77.9 nm, while more significant increases could be measured from 68.9 to 96.7 nm for $E_{74}F_{19}$-H_{300} and from 61.8 to 119 nm for $E_{94}F_{23}$-H_{300}. This could be explained that $E_{74}F_{19}$-H_{300} and $E_{94}F_{23}$-H_{300} contain almost a doubled PFBMA content than such in $E_{82}F_{10}$-H_{300}, which enables increasing NAC conjugation, making the resultant external hydrophilic layer denser and thicker, so increasing their ultimate DLS sizes.

In the next few investigations leading to the biological assessments, only NAC-bonded $E_{74}F_{19}$-H_{300} particles were investigated due to the higher numbers of NAC units (19 per chains at full conversion compared to 10 units/chain in $E_{82}F_{10}$-H_{300}) as the pharmacological effects would be expected to be higher for those particles. As importantly, particles could be prepared in that case with an optimal size range of approximately 100 nm and a relatively narrow distribution (PDI of 0.24) that facilitates cell internalization, [33,34] as well as with a ZP of −19 mV that provides an interparticle electrostatic repulsion large enough to enable the stability and long-term storage of NPs in water.

3.4.2. Conjugation of DOX onto $E_{74}F_{19}$-H_{300} particle surface using EDC/NHS activation reaction

DOX was grafted onto the particle surface by conjugating the NAC with DOX using a two-step carbodiimide activation chem-

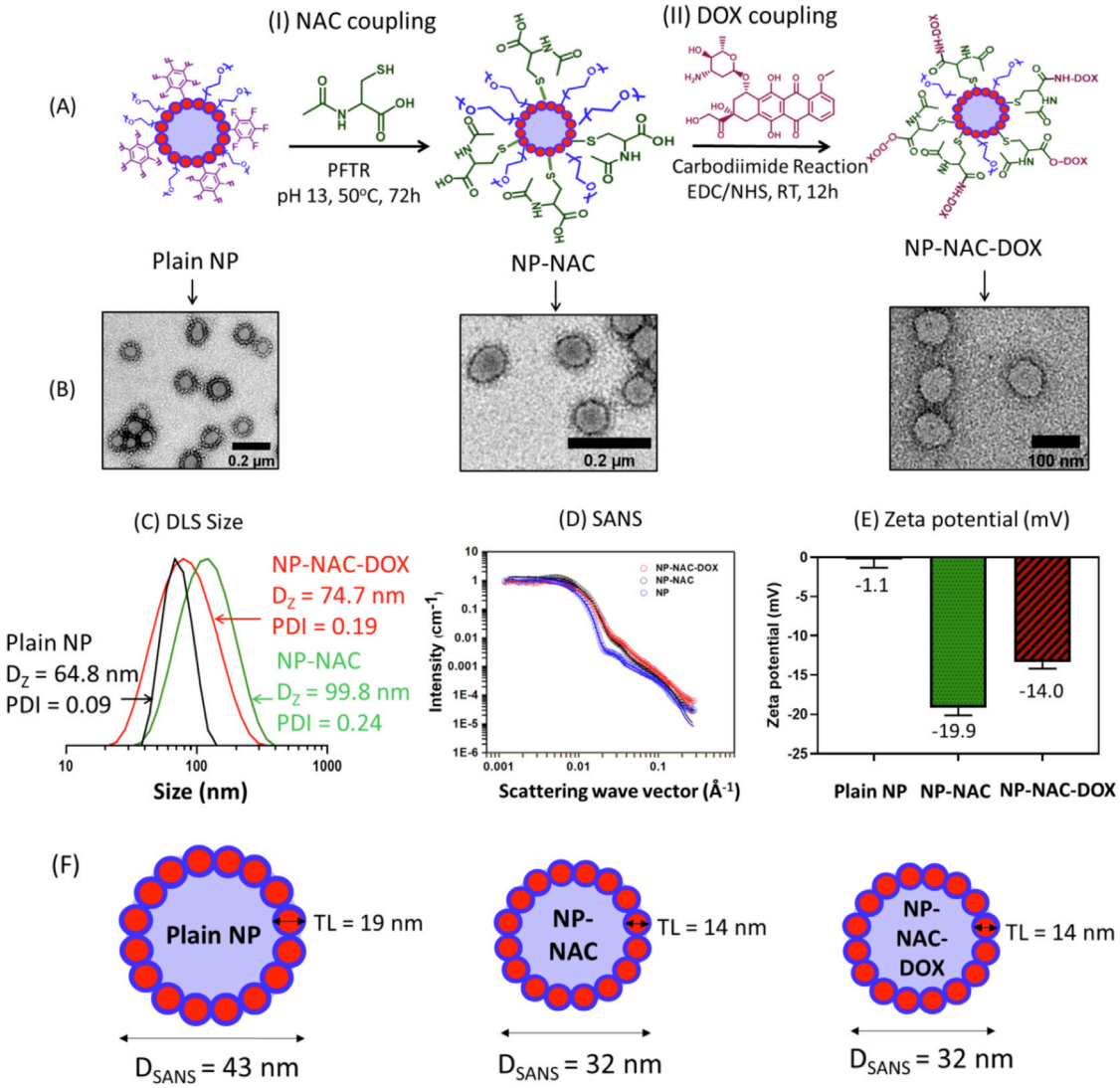

Fig. 6. (A) Illustration of particle surface functionalization with NAC and DOX; (B) TEM images of plain NP, NP-NAC and NP-NAC-DOX; (C) Normalized intensity DLS size of plain NP, NP-NAC, NP-NAC-DOX (NP-NAC:DOX = 1:5); (D) SANS spectra of NP, NP-NAC and NP-NAC-DOX fitted by raspberry-like model; (E) Zeta potential (mV). (F) Illustration of particle diameter (D_{SANS}) and thickness layer (TL) by SANS. Results are shown as the mean ± standard deviation of three replicates.

istry. [15] Figure SI8 displays the fluorescence spectra for different particle compositions: from the vesicle alone, to $E_{74}F_{19}$-H_{300}-NAC_{19}-DOX particles at molar ratio of 1:5, and free DOX.HCl was provided for comparison. As expected, NPs-NAC did not emit any light by fluorescence while NPs-NAC-DOX had a maximum emission corresponding to free DOX at 595 nm, confirming that DOX was incorporated on the particle surface. DOX integrated onto NP surface was quantified by comparing with the prepared calibration curve of DOX in DMSO (Figure SI7), resulting in the DOX concentration of 31 μg mL^{-1} and 153 μg mL^{-1} at the initial NP:DOX ratio of 1:1 and 1:5, respectively.

The particles remain the structures of vesicles despite the two functionalization steps, as confirmed by TEM in (Fig. 6B). The incorporation of DOX was also confirmed by the change of ZPs and sizes. Indeed, NPs-NAC had ZP of −19 mV, after coupling with DOX, ZP of NPs-NAC-DOX increased to −14 mV, showing that several carboxylic acid groups of NAC molecules were replaced by DOX, thus ZP values became less negative. In addition to the ZP difference, DLS measurements indicate that particle diameters increase after coupling with NAC, from 65 nm in plain NPs to 100 nm in NPs-NAC but decrease to 75 nm after DOX conjugation (Fig. 6C). The decrease in size of NPs-NAC-DOX is probably attributed to the addition of hydrophobicity of DOX onto the particle surface, and due to the hydrophobic effects, NPs are likely to shrink and reduce in sizes.

The stability of DOX-loaded NPs and NPs-NAC-DOX polymer-drug conjugates in the presence of bovine serum albumin (BSA) 0.2 wt% at 37 °C were undertaken by measuring their sizes over

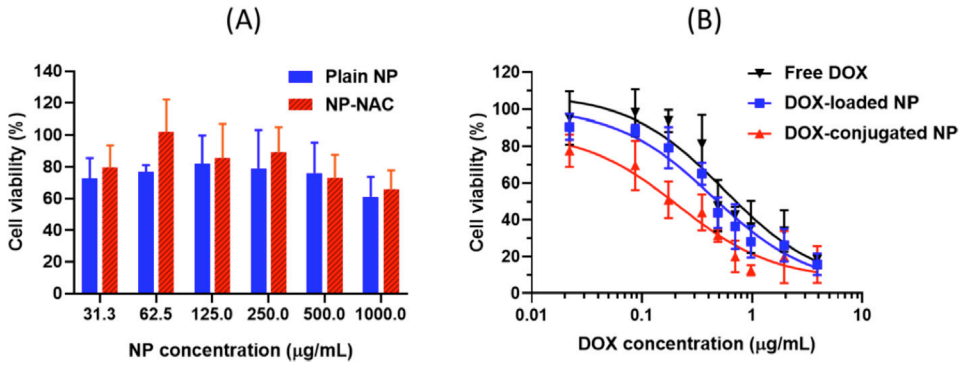

Fig. 7. (A) Cell viability of NPs and NP-NAC incubated with MDA-MB-231 cells (NP equivalent concentrations) for 72 h using MTT assay. (B) MDA-MB-231 cells upon incubation with free doxorubicin (free DOX.HCl), DOX-loaded NPs and DOX-conjugated NPs (NP-NAC-DOX) (DOX equivalent concentrations) after 72 h using AlamarBlue assay, curves fitted by non-linear regression [inhibitor]:response equation (three parameters) in GraphPad Prism 8.0.1. Results are shown as the mean ± standard deviation from two individual experiments with three replicates for each experiment (thus sample number N = (1 experiment, 3 wells) * 2 = 6).

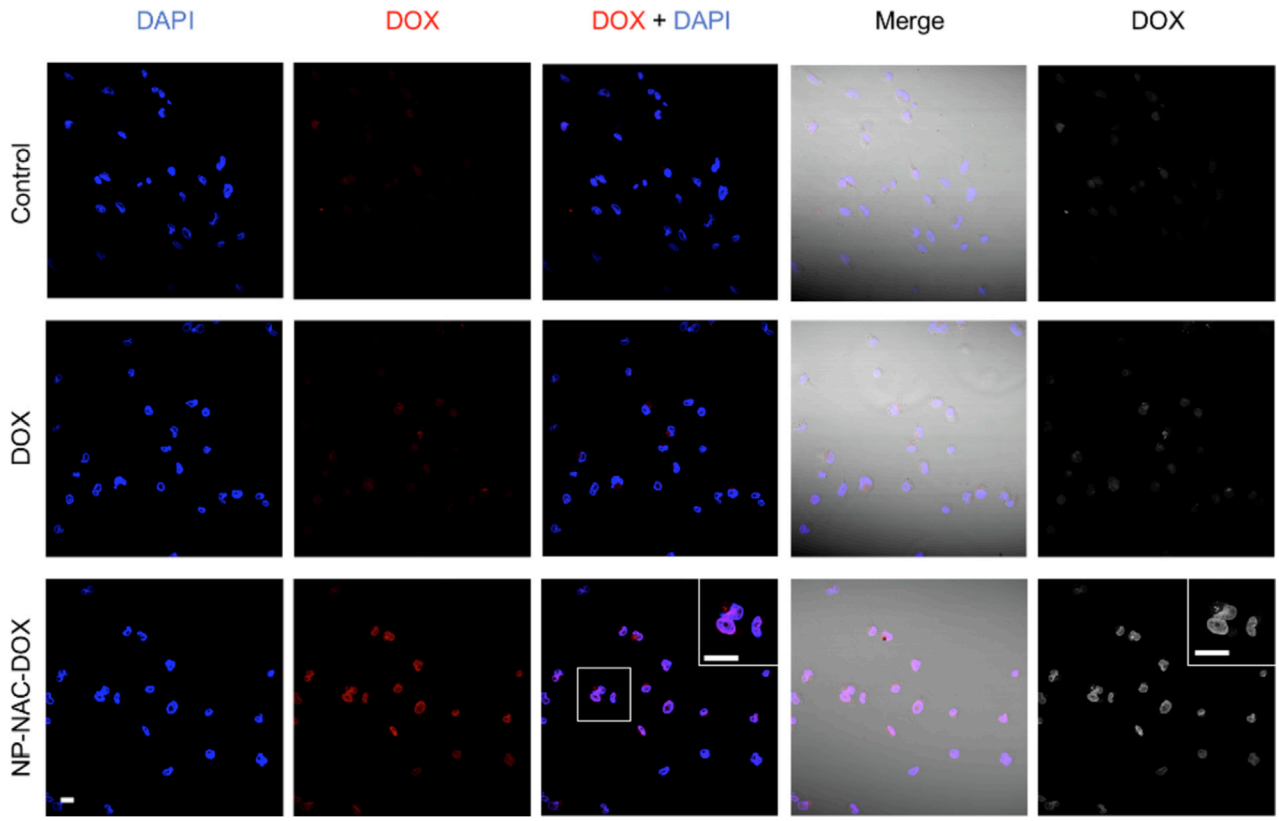

Fig. 8. Cellular uptake assessed by confocal microscopy in 2D monolayer of MDA-MB-231 cells with NPs-NAC-DOX after 5 h incubation. Nuclei stained with DAPI (Ex 350 nm/Em 470 nm), NPs-NAC-DOX (Ex 480 nm/Em 590 nm), Merged image from the superimposition of DAPI and DOX; Scale bar 20 μm. Results are shown as the mean ± standard deviation of three replicates from one experiment (sample number N = 3).

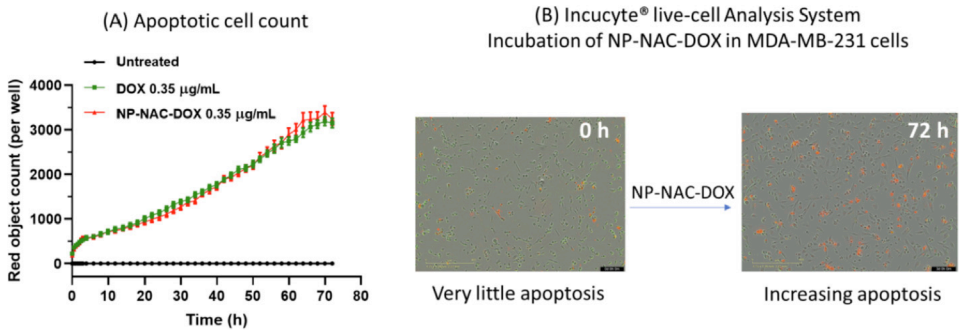

Fig. 9. Apoptosis assay by Incycute® live-cell analysis. (A) Annexin red-labelled apoptotic cell count vs. time of untreated cells (black), cells incubated with free DOX 0.214 μg mL^{-1} (green) and NP-NAC-DOX with DOX concentration of 0.214 μg mL^{-1} (red); (B) Images of distribution of red dying cells at 0 h and 72 h in the incubator upon treating with NP-NAC-DOX. Scale bar 400 μm. Results are shown as the mean ± standard deviation of three replicates from one experiment (N = 3).

72 h (Figure SI10). The incubation with BSA did not change particle size as compared to NPs without BSA in both groups of NPs, hence highlighting the high stability of the designed NPs against possible protein attachment and precipitation in plasma media.

3.4.3. Summary for in situ drug loading and post-PISA drug conjugation

Taken together, the PISA chain extension of $E_{74}F_{19}$ macro-CTA with HPMA monomer allows formation of drug-loaded NPs or PISA-made polymer-drug conjugates. However, to facilitate the particle characterization as well as calculation of drug release and cell culture experiments, polymer-drug conjugates will be further utilized due to their high grafted DOX concentration of 153 μg mL^{-1}, equivalent to 7.69 μg of conjugated DOX per 1 mg NP, as compared to 80 μg mL^{-1} of DOX concentration in DOX-loaded NPs, equivalent to 3.8 μg of loaded DOX per 1 mg NP. Therefore, $E_{74}F_{19}$-H_{300} plain NPs, and post-PISA functionalized NPs such as $E_{74}F_{19}$-H_{300}-NAC_{19}, and $E_{74}F_{19}$-H_{300}-NAC_{19}-DOX were selected for further characterizations and assessments. From now on $E_{74}F_{19}$-H_{300}, $E_{74}F_{19}$-H_{300}-NAC_{19}, and $E_{74}F_{19}$-H_{300}-NAC_{19}-DOX were referred to as NP, NP-NAC, and NP-NAC-DOX.

3.5. Small-angle neutron scattering (SANS)

SANS spectra of NP, NP-NAC and NP-NAC-DOX are presented in (Fig. 6D). Based upon TEM images, SANS spectra were fitted by a raspberry-like model by SAS view software. SANS confirms that the obtained particles are monodisperse with high stability and in the form of raspberry-shaped vesicles, as their curves fall perfectively in line with their corresponding fits by this model (Figure SI11). Overall, particle sizes from SANS are smaller than those measured by DLS. This is attributed to the different mechanisms of size measurement between these 2 techniques. DLS measures the average hydrodynamic diameters including the water layers associated on particle surfaces. [35] Nevertheless, SANS assesses the static colloidal structure by measuring the internal core size distribution of particles and excluding the external hydrophilic conjugation layer, hence giving smaller size values than those of DLS. [35] Furthermore, the functionalization of NAC and NAC + DOX decreases slightly particle core sizes compared to the lone NPs probably because the conjugation layers may compress the particle cores thus reducing their sizes.

3.6. Cytotoxicity and cellular uptake of NPs

3.6.1. Cytotoxicity

The cytotoxicity was undertaken in human triple-negative breast cancer cells MDA-MB-231 by evaluating the cell viability of NPs and NP-NAC using MTT assay (Fig. 7A) as well as free DOX, DOX-loaded NPs, and DOX-conjugated NPs using AlamarBlue assay (Fig. 7B). Fig. 8A exhibits that plain NPs and NP-NAC show over 80 % of cell viability, indicating that the DOX-free NPs are safe and biocompatible for biomedical applications.

On the other hand, DOX-loaded and DOX-conjugated NPs display a comparable cell death with free DOX, possessing IC_{50} values of 0.44 ± 0.22, 0.21 ± 0.13, and 0.561 ± 0.37 μg mL^{-1} ($p < 0.05$), respectively, (Fig. 7B). Thus, the encapsulation of DOX or incorporation of DOX onto particle surface shows the toxicity and inhibiting potency towards MDA-MB-231 cells.

3.6.2. Cell uptake

Due to the high conjugated DOX concentration (153 μg mL^{-1}) compared to such of encapsulated DOX (80 μg mL^{-1}), DOX-conjugated NPs or NP-NAC-DOX were selected for further cell uptake experiment. The confocal images in Fig. 8 indicate the presence of DOX fluorescence inside the MDA-MB-231 cell nuclei after 5 h of incubation with NP-coupled DOX, whereas very week signal of free DOX in the cell nuclei, suggesting that the polymer-DOX conjugates enhance the DOX retention in cancer cells. This is simply because free DOX is mostly penetrated through cell membrane *via* passive diffusion, while polymer-drug conjugates, due to their large sizes are typically internalized *via* endocytic mechanisms, contributing to higher uptake as compared to free DOX. [36]

3.6.3. Cell apoptosis assay by Incucyte® live-cell analysis system

DOX is a chemotherapeutic agent well-known to impart apoptosis and tumor cell death. Therefore, we examined the apoptotic activity of NP-NAC-DOX and free DOX in MDA-MB-231 cell lines with the help of Incucyte® live-cell analysis system, allowing to perform an automatic apoptosis assay at real time. Apoptotic cells express phosphatidylserine (PS) on their surfaces; thus, Annexin V red dye was used since it can bind to PS residues and enable the detection of dying cells. Fig. 9 exhibits the automatic quantification of Annexin V binding to apoptotic cells, indicating that DOX-conjugated NPs and free DOX result in the same number of red object count (per well) or the same number of Annexin-marked apoptotic cells per well upon incubating with MDA-MB-231 cells for 72 h, (Fig. 9A). NP-NAC-DOX is also associated with a significantly higher number of red apoptotic cells after 72 h, as compared to 0 h, as seen in Fig. 9B.

4. Conclusions

We have synthesized amphiphilic block co-polymers containing poly((ethylene glycol) methacrylate)–*co*-poly(pentafluorophenyl methacrylate)-*b*-poly(hydroxypropyl methacrylate) (P((PEGMA-

co-PFBMA)-*b*-PHPMA)) at 10 wt% by PISA. The block copolymer simultaneously self-assembled into NPs during PISA process inducing NPs of different sizes and shapes, transforming from spheres, cylinders to vesicles. We demonstrated that the length of hydrophilic blocks exerted an impact on final particle sizes and that increasing hydrophilicity while remaining the hydrophobicity made the obtained block copolymer NPs smaller. The ultimate vesicles were in the form of raspberries confirmed by SANS spectra and sized at 69 nm with PDI 0.02. DOX was directly loaded during PISA with acceptable encapsulation efficiencies. By tuning the macro-CTA block, the same PISA-made NPs could be incorporated with NAC and DOX using PFTR and carbodiimide reaction at high yields, respectively. The lone NPs and NP-conjugated NAC showed no significant cytotoxicity towards MDA-MB-231 cell lines, enabling their desirable safety and biocompatible profiles. Nonetheless, the *in situ* DOX loading or post-PISA polymer-DOX conjugates resulted in an incremental cell death with the increasing concentrations, whose IC_{50} values were almost similar to such of free DOX. The confocal microscopy indicated that polymer-DOX conjugates are internalized into tumor cells imparting higher cell uptake as compared to free DOX. NP-NAC-DOX caused a similar number of apoptotic cells as free DOX at the same DOX concentration over 72 h of incubation in the Incucyte® live-cell analysis system. Conclusively, we obtained a novel generation of block copolymer NPs that were simultaneously produced in a one-pot PISA technique at 10 wt%, enabling either *in situ* DOX loading by physical entrapping or post-polymerization surface functionalization of the obtained NPs with DOX, and possibly with targeting ligands in the future application. We also illustrated that critical reaction parameters of PISA, for example hydrophilicity/hydrophobicity ratio can be readily tuned to engineer NPs of favorable sizes, shapes, and colloidal stability meeting the requirements of biomedical applications. Based upon the versatility of PISA which allows either direct drug encapsulation or post-PISA polymer-drug conjugates, this study therefore, could potentially pave the way for new possibilities of incorporating PISA into drug delivery designs and biomaterials science. Further work might involve investigating the synthesis of NPs by PISA at higher concentrations of 20–30 wt% while attempting to encapsulate multimodal or multitherapeutic molecules, as well as surface functionalize with active ligands. It is also of importance to examine the synthesized nanomaterials in other types of tumors and later in *vivo* experiments.

Declaration of Competing Interest

The authors declare that they have no known competing financial interests or personal relationships that could have appeared to influence the work reported in this paper.

Acknowledgements

The authors gratefully acknowledge the financial support obtained from the Ministère de l'Enseignement supérieur, de la Recherche et de l'Innovation (MESRI) and Université Paris-Est Créteil. We thank Dr. Blandine Brissaut and Dr. Benoit Vallée for their insightful comments.

Author Contributions

HP was in charge of conceptualization, methodology, data curation, and writing- original draft. MC, CH, JC helped in biological studies. CLC and SP supported SANS. JP and BC supervised and reviewed the manuscript. All authors have given approval to the final version of the manuscript.

Appendix A. Supplementary material

Supplementary data to this article can be found online at

References

[1] A.K. Pearce, A.J. Blok, G. Yilmaz, N. Singh, R.J. Cavanagh, T. Abelha, V. Taresco, C. Alexander, Functional Polymers for Drug Delivery: prospects and Challenges, Chim. Oggi/Chemistry Today 36 (6) (2018) 38–42.
[2] H. Phan, R.I. Minut, P. McCrorie, C. Vasey, R.R. Larder, E. Krumins, M. Marlow, R. Rahman, C. Alexander, V. Taresco, A.K. Pearce, Role of Self-Assembly Conditions and Amphiphilic Balance on Nanoparticle Formation of PEG-PDLLA Copolymers in Aqueous Environments, J. Polym. Sci. Part A Polym. Chem. 57 (17) (2019) 1801–1810.
[3] N.J.W. Penfold, J. Yeow, C. Boyer, S.P. Armes, Emerging Trends in Polymerization-Induced Self-Assembly, ACS Macro Lett. 8 (8) (2019) 1029–1054.
[4] J.C. Foster, S. Varlas, B. Couturaud, J.R. Jones, R. Keogh, R.T. Mathers, R.K. O'Reilly, Predicting Monomers for Use in Polymerization-Induced Self-Assembly, Angew. Chemie - Int. Ed. 57 (48) (2018) 15733–15737.
[5] H. Phan, V. Taresco, J. Penelle, B. Couturaud, Polymerisation-Induced Self-Assembly (PISA) as a Straightforward Formulation Strategy for Stimuli-Responsive Drug Delivery Systems and Biomaterials: recent Advances, Biomater. Sci. 9 (1) (2021) 38–50.
[6] M. Lansalot, J. Rieger, Polymerization-Induced Self-Assembly, Macromol. Rapid Commun. 40 (2) (2019) 1–3.
[7] S.L. Canning, G.N. Smith, S.P. Armes, A Critical Appraisal of RAFT-Mediated Polymerization-Induced Self-Assembly, Macromolecules 49 (6) (2016) 1985–2001.
[8] Y. Kwon, Possible Beneficial Effects of N-Acetylcysteine for Treatment of Triple-Negative Breast Cancer, Antioxidants 10 (2) (2021) 169.
[9] J.H. Doroshow, G.Y. Locker, I. Ifrim, C.E. Myers, Prevention of Doxorubicin Cardiac Toxicity in the Mouse by N-Acetylcysteine, J. Clin. Invest. 68 (4) (1981) 1053–1064.
[10] J.-M. Noy, A.-K. Friedrich, K. Batten, M.N. Bhebhe, N. Busatto, R.R. Batchelor, A. Kristanti, Y. Pei, P.J. Roth, Para-Fluoro Postpolymerization Chemistry of Poly (Pentafluorobenzyl Methacrylate): modification with Amines, Thiols, and Carbonylthiolates, Macromolecules 50 (18) (2017) 7028–7040.
[11] N. Busatto, J.L. Keddie, P.J. Roth, Sphere-to-Worm Morphological Transitions and Size Changes through Thiol-: para -Fluoro Core Modification of PISA-Made Nano-Objects, Polym. Chem. 11 (3) (2020) 704–711.
[12] N. Busatto, V. Stolojan, M. Shaw, J.L. Keddie, P.J. Roth, Reactive Polymorphic Nanoparticles: Preparation via Polymerization-Induced Self-Assembly and Postsynthesis Thiol–Para-Fluoro Core Modification, Macromol. Rapid Commun. 40 (2) (2019) 1–6.
[13] H. Turgut, A.C. Schmidt, P. Wadhwani, A. Welle, R. Müller, G. Delaittre, The Para-Fluoro-Thiol Ligation in Water, Polym. Chem. 8 (8) (2017) 1288–1293.
[14] B. Couturaud, P.G. Georgiou, S. Varlas, J.R. Jones, M.C. Arno, J.C. Foster, R.K. O'Reilly, Poly(Pentafluorophenyl Methacrylate)-Based Nano-Objects Developed by Photo-PISA as Scaffolds for Post-Polymerization Functionalization, Macromol. Rapid Commun. 40 (2) (2019).
[15] N. Nakajima, Y. Ikada, Mechanism of Amide Formation by Carbodiimide for Bioconjugation in Aqueous Media, Bioconjug. Chem. 6 (1) (1995) 123–130.
[16] I. Chaduc, W. Zhang, J. Rieger, M. Lansalot, F. D'Agosto, B. Charleux, Amphiphilic Block Copolymers from a Direct and One-Pot RAFT Synthesis in Water, Macromol. Rapid Commun. 32 (16) (2011) 1270–1276.
[17] F. Coumes, M. Balarezo, J. Rieger, F. Stoffelbach, Biobased Amphiphilic Block Copolymers by RAFT-Mediated PISA in Green Solvent, Macromol. Rapid Commun. 41 (9) (2020) 2000002.
[18] B. Ebeling, K. Belal, F. Stoffelbach, P. Woisel, M. Lansalot, F. D'Agosto, Polymer Nanospheres with Hydrophobic Surface Groups as Supramolecular Building Blocks Produced by Aqueous PISA, Macromol. Rapid Commun. 40 (2) (2019) 1800455.
[19] S. Shen, E.D. Sudol, M.S. El-Aasser, Control of Particle Size in Dispersion Polymerization of Methyl Methacrylate, J. Polym. Sci. Part A Polym. Chem. 31 (6) (1993) 1393–1402.
[20] R.S. Lee, Y.T. Huang, Tuning the Hydrophilic-Hydrophobic Balance of Block-Graft Copolymers by Click Strategy: Synthesis and Characterization of Amphiphilic PCL-b-(PαN3 CL-g-PBA) Copolymers, Polym. J. 42 (4) (2010) 304–312.
[21] Y. Yang, A. Alford, V. Kozlovskaya, S. Zhao, H. Joshi, E. Kim, S. Qian, V. Urban, D. Cropek, A. Aksimentiev, E. Kharlampieva, Effect of Temperature and Hydrophilic Ratio on the Structure of Poly(N -Vinylcaprolactam)- Block -Poly (Dimethylsiloxane)- Block -Poly(N -Vinylcaprolactam) Polymersomes, ACS Appl. Polym. Mater. 1 (4) (2019) 722–736.
[22] D. Chenthamara, S. Subramaniam, S.G. Ramakrishnan, S. Krishnaswamy, M.M. Essa, F.-H. Lin, M.W. Qoronfleh, Therapeutic Efficacy of Nanoparticles and Routes of Administration, Biomater. Res. 23 (1) (2019) 20.
[23] R. Abellan-Pose, C. Teijeiro-Valiño, M.J. Santander-Ortega, E. Borrajo, A. Vidal, M. Garcia-Fuentes, N. Csaba, M.J. Alonso, Polyaminoacid Nanocapsules for Drug Delivery to the Lymphatic System: effect of the Particle Size, Int. J. Pharm. 509 (1–2) (2016) 107–117.

[24] F. D'Agosto, J. Rieger, M. Lansalot, RAFT-Mediated Polymerization-Induced Self-Assembly, Angew. Chemie Int. Ed. 59 (22) (2020) 8368–8392.
[25] C.A. Figg, A. Simula, K.A. Gebre, B.S. Tucker, D.M. Haddleton, B.S. Sumerlin, Polymerization-Induced Thermal Self-Assembly (PITSA), Chem. Sci. 6 (2) (2015) 1230–1236.
[26] M. Guerre, G. Lopez, B. Améduri, M. Semsarilar, V. Ladmiral, Solution Self-Assembly of Fluorinated Polymers, an Overview, Polym. Chem. 12 (27) (2021) 3852–3877.
[27] W.M. Wan, C.Y. Pan, One-Pot Synthesis of Polymeric Nanomaterials via RAFT Dispersion Polymerization Induced Self-Assembly and Re-Organization, Polym. Chem. 1 (9) (2010) 1475–1484.
[28] J.C. Foster, S. Varlas, B. Couturaud, Z. Coe, R.K. O'Reilly, Getting into Shape: Reflections on a New Generation of Cylindrical Nanostructures' Self-Assembly Using Polymer Building Blocks, J. Am. Chem. Soc. 141 (7) (2019) 2742–2753.
[29] S. Varlas, J.C. Foster, P.G. Georgiou, R. Keogh, J.T. Husband, D.S. Williams, R.K. O'Reilly, Tuning the Membrane Permeability of Polymersome Nanoreactors Developed by Aqueous Emulsion Polymerization-Induced Self-Assembly, Nanoscale 11 (26) (2019) 12643–12654.
[30] H. Asem, W. Zheng, F. Nilsson, Y. Zhang, M.S. Hedenqvist, M. Hassan, E. Malmström, Functional Nanocarriers for Drug Delivery by Surface Engineering of Polymeric Nanoparticle Post-Polymerization-Induced Self-Assembly, ACS Appl. Bio Mater. 4 (1) (2021) 1045–1056.
[31] J. Engström, H. Asem, H. Brismar, Y. Zhang, M. Malkoch, E. Malmström, In Situ Encapsulation of Nile Red or Doxorubicin during RAFT-Mediated Emulsion Polymerization via Polymerization-Induced Self-Assembly for Biomedical Applications, Macromol. Chem. Phys. 221 (5) (2020) 1900443.
[32] E.P. Serjeant, B. Dempsey, Ionisation Constants of Organic Acids in Aqueous Solution, Int. Union Pure Appl. Chem. 23 (1979) 26.
[33] L. Shang, K. Nienhaus, X. Jiang, L. Yang, K. Landfester, V. Mailänder, T. Simmet, G.U. Nienhaus, Nanoparticle Interactions with Live Cells: quantitative Fluorescence Microscopy of Nanoparticle Size Effects, Beilstein J. Nanotechnol. 5 (1) (2014) 2388–2397.
[34] N. Hoshyar, S. Gray, H. Han, G. Bao, The Effect of Nanoparticle Size on in Vivo Pharmacokinetics and Cellular Interaction, Nanomedicine 11 (6) (2016) 673–692.
[35] F. Bouanani, D. Bendedouch, J. Teixeira, L. Marx, P. Hemery, Characterization of a Miniemulsion by DLS and SANS, Colloids Surfaces A Physicochem. Eng. Asp. 404 (2012) 47–51.
[36] T. Lei, S. Srinivasan, Y. Tang, R. Manchanda, A. Nagesetti, A. Fernandez-Fernandez, A.J. McGoron, Comparing Cellular Uptake and Cytotoxicity of Targeted Drug Carriers in Cancer Cell Lines with Different Drug Resistance Mechanisms. *Nanomedicine Nanotechnology*, Biol. Med. 7 (3) (2011) 324–332.